RESEARCH ARTICLE | MARCH 23 2026

# Anion photoelectron spectroscopy of the hydrogen iodide anion, $HI^-$

Tatsuya Chiba ; Burak A. Tufekci ; Shiying Wang ; Yuheng Han ; Kit H. Bowen



*J. Chem. Phys.* 164, 124303 (2026)
https://doi.org/10.1063/5.0327095
CHORUS

The Journal of Chemical Physics ARTICLE pubs.aip.org/aip/jcp

# Anion photoelectron spectroscopy of the hydrogen iodide anion, $HI^-$

Cite as: J. Chem. Phys. 164, 124303 (2026); doi: 10.1063/5.0327095
Submitted: 10 February 2026 • Accepted: 9 March 2026 •
Published Online: 23 March 2026



Tatsuya Chiba, Burak A. Tufekci, Shiying Wang, Yuheng Han, and Kit H. Bowen[a]

## AFFILIATIONS

Department of Chemistry, Johns Hopkins University, Baltimore, Maryland 21218, USA

[a]Author to whom correspondence should be addressed: kbowen@jhu.edu

## ABSTRACT

Among the hydrohalic acids, only hydrogen iodide (HI) forms its parent anion. $HI^-$ was identified mass spectrometrically, having been seen in three different anion-forming environments. In this work, $HI^-/DI^-$ anions were produced by Rydberg electron transfer using electronically excited $K^{**}(8d)$ atoms as HI/DI collision partners, after which their anion photoelectron spectra (aPES) were measured using both magnetic bottle and velocity map imaging electron energy analyzers. The electron affinities (EA) of HI and DI were determined to be EA(HI) = 0.051 ± 0.015 eV and EA(DI) = 0.028 ± 0.020 eV, while the bond dissociation energies ($D_0$) of their respective anions were determined to be $D_0(HI^-)$ = 0.045 ± 0.015 eV and $D_0(DI^-)$ = 0.063 ± 0.020 eV. Analysis of the vibrational structure in their aPES revealed that these anions possess double-well potentials, with their vibrational wavefunctions ranging over the two wells via tunneling. Franck–Condon analysis identified the bond lengths at the two minima of the double-well potential to be ~2.03 and ~2.37 Å. Thus, $HI^-$ and $DI^-$ each exist in two forms. In addition to these valence-bound $HI^-$ and $DI^-$ anions, the existence of non-valence-bound $HI^-$ (and perhaps $DI^-$) species was implied by weak but persistent shoulder-like photoelectron signals at extremely low electron binding energies. Comparison of the anion photoelectron spectrum of $HI^-$ with those of alkali halide anions, $MX^-$, supported the covalent character of the H–I chemical bond.





## I. INTRODUCTION

Hydrogen iodide (HI), the strongest acid among the hydrohalic acids (HX), has been studied extensively, for example, by photoelectron spectroscopy,[1–12] Penning ionization electron spectroscopy,[3,13] photoionization electron spectroscopy,[14] photoionization mass spectrometry,[15] electron coincidence spectroscopy,[16] resonance-enhanced multiphoton ionization spectroscopy (REMPI),[17] pulsed-field ionization zero electron kinetic energy (PFI-ZEKE) spectroscopy,[18] UV absorption spectroscopy,[19–21] UV photodissociation spectroscopy,[22–24] IR spectroscopy,[25,26] Raman spectroscopy,[27] rotational spectroscopy,[28–31] *ab initio* calculations,[32–35] and time-dependent wave-packet calculations.[36,37] Nevertheless, despite the many studies of the neutral HI molecule and of its neutral hydrohalic acid siblings, only hydrogen iodide among them forms its parent anion, that is, $HI^-$. Electron attachment to single, neutral HX molecules generally results in the appearance of $X^-$ anions, these having been formed through dissociative electron attachment (DEA).[38,39] Note that HI has both DEA and parent anion-forming channels.

The first observation of $HI^-$ as a long-lived anion was made by Chupka *et al.* in 1982.[40] They observed $HI^-$ in mass spectra by introducing HI gas into a Penning discharge ion source. That observation meant that $HI^-$ has a potential well deep enough to support at least one vibrational level and, assuming that it was stable rather than metastable, that the vibrational ground state lies below the $H + I^-$ dissociation limit. That set the energetic requirement for the electron affinity (EA) of HI to be: $EA(HI) > EA(I) - D_0(HI) = 6$ meV.[40] Then, in 1993, Compton *et al.* formed $HI^-$ and $DI^-$ by Rydberg electron transfer (RET) using highly excited alkali metal atoms, $HI + M^{**} \rightarrow HI^- + M^+$.[41] In their experiments, a HI molecular beam collided with excited alkali metal atoms, $M^{**}$ (M = Na, Rb, Cs), that had been selectively laser-excited to *n*s and *n*d Rydberg electronic states with principal quantum numbers ranging over $n$ = 8–40. The collision-induced electron transfer produced $HI^-$ for $n < 13$, as well as $I^-$ formed by dissociative electron attachment. These investigators set a lower bound for the $HI^-$ lifetime to be ~1 ms based on their mass spectrometric observations. Then, in 1996, Tuinman and Compton mass spectrometrically observed $HI^-$ formation due to DEA of 2-iodomethane.[42] Neither $HCl^-$ nor $HBr^-$ were observed when

2-chloropropane and 2-bromopropane were respectively subjected to DEA.

The potential energy curve of $HI^-$ had been investigated via *ab initio* calculations in 1988.[43] In an indirect manner, DEA experiments on HI had also provided information on the $HI^-$ potential.[44–49] Specifically, DEA of HI using low-energy electrons (0–170 meV) that had been produced by photoionization of Ar atoms and Rydberg-excited $Ar^{**}$ atoms,[49] followed by analysis with a non-local resonance model,[50–52] mapped the resonance potential of $HI^-$. At higher electron energy (>6 eV), $HI^-$ Feshbach resonances were observed in electron transmission spectra.[53] These electron scattering experiments provided information on $HI^-$ temporary negative ions (TNI) as shape and Feshbach resonances. The observation of stable $HI^-$ anions, however, was limited to the work described above.[40–42]

In this work, $HI^-$ and $DI^-$ parent anions were produced by RET from selectively laser-excited potassium atoms following Compton *et al.*'s procedure.[41] Anion photoelectron spectroscopy (aPES) was performed on them using both magnetic bottle (MB) and velocity map imaging (VMI) electron energy analyzers. The recorded photoelectron spectra showed clear vibrational progressions due to transitions from the ground-state anion to the ground state of neutral HI ($X\ ^1\Sigma^+$), as well as a broad feature due to a transition to neutral HI's first excited state ($a^3\Pi_1$). The electron affinities (EA) were determined to be EA(HI) = 0.051 ± 0.015 eV and EA(DI) = 0.028 ± 0.020 eV, while the bond dissociation energies ($D_0$) of the anions were determined to be $D_0(HI^-)$ = 0.045 ± 0.015 eV and $D_0(DI^-)$ = 0.063 ± 0.020 eV. The vibrational structure in the anion photoelectron spectra revealed that $HI^-$ possesses a double-well potential, with its vibrational wavefunctions ranging over the two wells via tunneling. Franck–Condon analysis showed that the bond lengths of $HI^-$ at the two minima of the double-well potential are 2.03 and 2.37 Å. Thus, $HI^-$ and $DI^-$ each exist in two forms.

## II. METHODS

### A. Preparation of HI gas

HI gas was obtained by dehydrating aqueous hydriodic acid, HI(aq), in a glassware apparatus under vacuum.[54] There, 5 ml of aqueous hydriodic acid (57 wt. %, stabilized, Sigma-Aldrich) was dripped from a dropping funnel onto an excess of phosphorus pentoxide located in a flask cooled by an ice-water bath. Phosphorus pentoxide caused the dehydration reaction, $P_4O_{10} + 6\ H_2O \rightarrow 4\ H_3PO_4$, and released gaseous hydrogen iodide. The resultant HI gas was further dehydrated by sending it through glass tubes packed with phosphorus pentoxide. The dried HI gas was condensed into a sample gas cylinder cooled by liquid nitrogen. Lastly, helium was added to the gas cylinder to make a HI/He (5%/95%) gas mixture.

### B. Preparation of DI(aq)

Aqueous deuterated hydriodic acid, DI(aq), was synthesized via the chemical reaction, $D_3PO_4(aq) + KI \rightarrow DI(aq) + KD_2PO_4$.[19] Initially, 10 ml of deuterated phosphoric acid $D_3PO_4$ (D 98%, 85% in $D_2O$, Sigma-Aldrich) and 10 g of potassium iodide were added to a vacuum-sealable stainless-steel container. Then, after evacuating the container, its temperature was slowly increased to 100 °C and held there for two hours. Next, the temperature was raised to 150 °C and held there for another hour, resulting in the formation of DI(aq) vapor. The vapor of DI(aq) was frozen into a separate, liquid-nitrogen-cooled stainless-steel container. This DI(aq) solution was used to produce $DI^-$, as described in Sec. II C.

### C. Anion formation and anion photoelectron spectroscopy (aPES)

The formation of $HI^-$ and $DI^-$ and the measurement of their anion photoelectron spectra were conducted on our apparatus, which consists of a Rydberg electron transfer (RET) ion source and its two dye lasers, a time-of-flight mass spectrometer (TOF-MS), a Nd:YAG photodetachment laser, a magnetic bottle electron energy analyzer (MB), and a velocity map imaging electron energy analyzer (VMI). The apparatus, described briefly here, is described in detail elsewhere.[55–57] $HI^-$ and $DI^-$ anions were formed by our Rydberg electron transfer (RET) ion source.[41] Here, we explain the experimental procedure for $HI^-$ first. A HI/He gas mixture (0 psig) was introduced via a pulsed valve (Parker–Hannifin) at 10 Hz. The HI molecular beam was cooled by supersonic expansion. After passing through a skimmer, the HI molecular beam collided with potassium atoms $K^{**}$ that had been laser-excited to selected Rydberg levels via two separate photon excitations. The effusive beam of potassium atoms from a 150 °C oven had been irradiated by 767 nm photons from the first of two dye lasers (Sirah Lasertechnik, Cobra, LDS751 in ethanol) before being irradiated by 457–497 nm photons from the second dye laser (Sirah Lasertechnik, Cobra-Stretch, Coumarin 480 in ethanol). The first laser excited the potassium atoms from the ground state to the first excited state ($^2P_{3/2}$ [Ar] $4p^1$), while the second laser further excited them selectively from the first excited state to the 8d–32d and 10s–33s Rydberg electronic states. This is a two-step process. The energy levels of potassium were those found in the NIST Atomic Spectra Database.[58] Collisions of HI with Rydberg-excited potassium $K^{**}$ formed $HI^-$ anions via Rydberg electron transfer through the reaction $HI + K^{**} \rightarrow HI^- + K^+$, as well as forming $I^-$ via DEA. The resultant $HI^-$ anions were extracted and mass-analyzed/selected via a Wiley–McLaren-type in-line time-of-flight mass spectrometer.

The anion photoelectron spectra of $HI^-$ formed by RET from $K^{**}$(8d) were measured by two distinct electron energy analyzers: a magnetic bottle (MB) and velocity map imaging (VMI). In the MB case, $HI^-$ was photodetached by the first, second, third, and fourth harmonic outputs of a Nd:YAG laser (Continuum, Surelite I-20; 1064, 532, 355, and 266 nm, respectively) after mass-gating and deceleration. The resolution of our magnetic bottle analyzer was ~35 meV at an electron kinetic energy of 1 eV. In the VMI case, after mass-gating, $HI^-$ was photodetached by the linearly polarized first and second harmonic outputs of a Nd:YAG laser (Continuum, Surelite I-20; 1064 and 532 nm, respectively). The resultant photodetached electrons were then accelerated toward a position-sensitive microchannel plate detector with a phosphor screen coupled to a CCD camera. The recorded two-dimensional images were symmetrized and inverse-Abel transformed via the BASEX method[59] to reconstruct the three-dimensional distributions of the photodetached electrons. The kinetic energies of the electrons were obtained from the reconstructed velocity map images

(resolution $\Delta E/E \sim 0.03$). In experiments using both MB and VMI electron energy analyzers, the recorded electron kinetic energies (EKE) were converted to electron binding energies (EBE) by the energy-conserving relationship: $h\nu$ = EBE + EKE, where $h\nu$ is the photon energy of the photodetachment laser. Photoelectron spectra measured using the magnetic bottle were calibrated using the well-known atomic transitions of $Pb^-$,[60,61] $Pd^-$,[62,63] $Cr^-$,[62,64] and $W^-$[62,65,66] when using 1064 nm photons [shown as Fig. S1(a) in the supplementary material]; $Pb^-$[60,61] when using 532 nm photons; and $Cu^-$[67] when using 355 and 266 nm photons. In the same way, photoelectron spectra measured using velocity map imaging were calibrated using the transitions of $Pb^-$, $Pd^-$, and $W^-$ when using 1064 nm photons [shown as Fig. S1(b) in the supplementary material] and $Pb^-$ when using 532 nm photons.

The molecular beam of DI was formed by placing a drop of deuterated hydriodic acid DI(aq) in the pulse valve filled with helium buffer gas (0 psig) and directing its vapor to the Rydberg electron transfer ion source. The anion photoelectron spectra of $DI^-$ formed by RET [$DI + K^{**}(8d) \rightarrow DI^- + K^+$] were measured by the magnetic bottle electron energy analyzer using the first and the second harmonic outputs of a Nd:YAG laser (1064 and 532 nm, respectively) after mass-gating and deceleration.

Note that analogous experiments were also performed for HCl and HBr. Pulsing HCl or HBr molecular beams into the RET ion source produced neither $HCl^-$ or $HBr^-$, nor, interestingly, $Cl^-$ or $Br^-$. These results are presented in the supplementary material.

### D. Franck–Condon simulation

According to the Franck–Condon principle, the probability of the transition, $M^-(v'') \rightarrow M(v') + e^-$, is proportional to $|M_e|^2|\langle\Psi_{v''}|\Psi_{v'}\rangle|^2$, where $M_e$ is the electric transition dipole moment and $|\langle\Psi_{v''}|\Psi_{v'}\rangle|^2$ is the Franck–Condon (F–C) factor that represents the spatial overlap between the vibrational wavefunctions of the anion and the neutral.[68,69] In the Condon approximation, $|M_e|^2$ can be treated as a constant for a given electronic transition. Therefore, the F–C factor represents the relative transition probabilities of a vibrational series in a given electronic transition. The F–C factors for HI ($v'$ = 0–10) ← $HI^-$ ($v''$ = 0) and DI ($v'$ = 0–14) ← $DI^-$ ($v''$ = 0) were calculated using the LEVEL16 program.[70] It was assumed that the potential energy curves are isotope-invariant; that is, HI and DI share the same potential energy curve. The generalized Morse potential (see Ref. 71) was employed for the HI neutral. This potential has been utilized in UV spectroscopic studies of HI.[22–24,36,37] For the potential energy curve of the $HI^-$ anion, a harmonic potential was used. A harmonic potential has three parameters: the depth of the well $D_e$, the force constant $k_e$, and the equilibrium bond length $r_e$. The $D_e$ and $k_e$ were determined based on the electron affinity values by a procedure described in Sec. III D. The $r_e$ was optimized so that the F–C simulation reproduces the relative intensity distribution of the vibrational progression in the experimental anion photoelectron spectra.

The photodetachment cross section $\sigma$ depends on the electron kinetic energy (EKE). In photodetachment from an atomic anion, this relation is described by Wigner's threshold law: $\sigma(\text{EKE}) \propto k^{2l+1}$, where $k = (2m_e \cdot \text{EKE})^{1/2}/\hbar$ is the magnitude of the linear momentum of the photoelectron and $l$ is the angular momentum of the outgoing electron.[72] The corresponding relationship for a diatomic anion was formulated by Geltman as follows: $\sigma(\text{EKE}) \approx (\text{const.}) \cdot \nu k^m$, where $\nu$ is the photon frequency and $m$ is an integer determined by the molecular symmetry and the molecular-axis component of the angular momentum of the molecular orbital from which the electron was photodetached.[73] We assumed that the photodetached electrons in the 1064 and 532 nm aPES originated from the σ orbital of $HI^-$, based on the electronic configuration of $HI^-$ ($X\ ^2\Sigma^+$, $1\sigma^2 2\sigma^2 1\pi^4 3\sigma^1$) used in a prior *ab initio* calculation[43] (see Fig. S2 in the supplementary material for the MO diagram). For photodetachment from a σ orbital of the heteronuclear diatomic anion, $m$ = 1 is used.[73] Therefore, the dependence of the photodetachment cross section on EKE in this case is $\sigma(\text{EKE}) \approx (\text{const.}) \cdot k \propto \text{EKE}^{1/2}$. To incorporate this relationship into the simulated spectra, the calculated F–C factors were multiplied by $\text{EKE}^{1/2}$. The resultant stick spectra were broadened by Gaussian functions to reproduce the experimental anion photoelectron spectra with a typical FWHM of 40–80 meV.

## III. RESULTS

### A. Formation of $HI^-$ and $DI^-$ by Rydberg electron transfer

Mass spectra of the anions formed by Rydberg electron transfer to HI from $K^{**}$ at 8d, 10d, and 32d Rydberg states are shown in Fig. 1(a). $I^-$ was observed by DEA of HI at all the Rydberg levels. With $K^{**}(8d)$, the ion signal of $HI^-$ ($m/z$ = 128) was observed along with that of $I^-$. The typical flight time of $HI^-$ in our TOF-MS was ~69 μs. As shown in Fig. 1(b), the ratio of $HI^-$ vs $I^-$ ion intensity (as determined by TOF peak area) decreased steadily with increasing principal quantum numbers of the $K^{**}$ Rydberg level until 14d/15s. This result is consistent with the observations of Compton *et al.*[41] Interestingly, the decrease of the $HI^-/I^-$ ion intensity ratio was not monotonic after $K^{**}(15d)$.

The mass spectrum obtained by adding DI(aq) to the pulse valve and directing its vapor into the RET ion source at $K^{**}(8d)$ is shown in Fig. 1(c). A peak for $DI^-$ ($m/z$ = 129) was observed, along with a peak for $HI^-$ in the same mass spectrum. The latter was due to residual HI in the gas line or to isotope exchange between the aqueous $DI/D_2O$ solution and $H_2O$ in the atmosphere while the solution was exposed to the air.

### B. Anion photoelectron spectra measured by the magnetic bottle (MB) electron energy analyzer

The anion photoelectron spectra of $HI^-$ measured with 1064 and 532 nm photons using our magnetic bottle electron energy analyzer are shown in Fig. 2(a), and the electron binding energies of all the observed peaks are summarized in Table I. Anion photoelectron spectroscopy measures the energy from the initial anionic state to the final neutral state. When the probed anion is cold—i.e., cooled by supersonic expansion and in its electronic and vibrational ground state—the recorded spectrum reflects the electronic and vibrational energy levels of the corresponding neutral. Hereafter in this discussion, a transition from the anion in a $v''$ vibrational state to the neutral in a $v'$ vibrational state ($v' \leftarrow v''$) is denoted as ($v'$, $v''$). The 1064 nm spectrum exhibited a vibrational peak progression corresponding to the transitions: (0, 0)–(3, 0), with the spacings between the adjacent peaks being consistent with the known

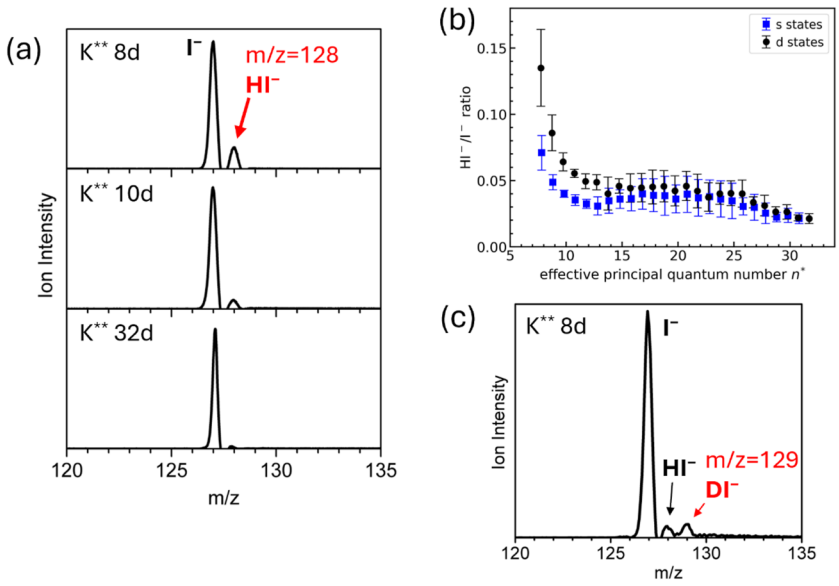


**FIG. 1.** (a) Mass spectra obtained by Rydberg electron transfer to HI from K** at 8d, 10d, and 32d Rydberg states. (b) Ion intensity ratio $HI^-/I^-$ plotted by the effective principal quantum number $n^* = n - \delta_{lj}$ of K** atoms excited to the 8d–32d and 10s–33s Rydberg states. The quantum defect $\delta_{lj}$ was taken from Ref. 74. (c) Mass spectrum showing $DI^-$ formed by Rydberg electron transfer from K** in its 8d Rydberg state.

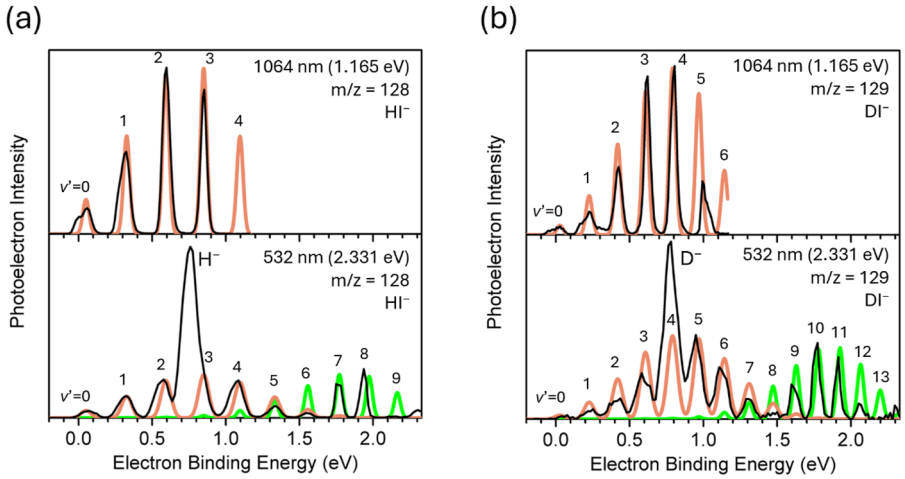


**FIG. 2.** Anion photoelectron spectra recorded by the magnetic bottle electron energy analyzer with 1064 nm (1.165 eV) and 532 nm (2.331 eV) photons for (a) $HI^-$ and (b) $DI^-$. The black lines are the experimental spectra, and the electron binding energies of each of the peaks are shown in Tables I and II. The orange curves show the results of Franck–Condon simulations for the transitions from $HI^-/DI^-$ ($v'' = 0$) in the inner well ($r_e$ = 2.03 Å) to HI/DI ($X\ ^1\Sigma^+$, $v'$). The green curves show the results of Franck-Condon simulations for the transitions from $HI^-/DI^-$ ($v'' = 0$) in the outer well ($r_e$ = 2.37 Å) to HI/DI ($X\ ^1\Sigma^+$, $v'$).

vibrational energy spacings of the HI ground state ($X\ ^1\Sigma^+$).[75] The (4, 0) peak had been expected to appear at the high electron binding energy edge of the 1064 nm spectrum but was absent because of the reduced electron transmission for low kinetic energy electrons in the magnetic bottle electron energy analyzer. Transitions from vibrationally excited anions (hot bands) were not observed. The 532 nm spectrum showed the same vibrational progression envelope but over an extended binding energy range from (0, 0) through (6, 0). The (3, 0) peak was hidden by an intense peak at 0.758 eV. That peak originated from a two-photon process: photodissociation of $HI^-$ to $H^-$ + I by the 532 nm photon, followed by the photodetachment of $H^-$. The electron binding energy of that peak agrees with the EA value of the H atom (0.754 eV[76]). Based on the relative energies of the $H(^2S) + I^-(^1S)$ and the $H^-(^1S) + I(^2P_{3/2})$ dissociation limits shown in Fig. 3, a photon energy of at least EA(I) − EA(H) = 2.305 eV is required to photodissociate $HI^-$ to $H^-$ + I. That is consistent with the appearance of the $H^-$ photoelectron peak in the 532 nm ($h\nu$ = 2.331 eV) photoelectron spectrum and its absence in the 1064 nm ($h\nu$ = 1.165 eV) spectrum. Beyond the energy of the (6, 0) peak at 1.544 eV, two peaks were observed at electron binding energies corresponding to the (7, 0) and (8, 0) transitions. Interpretation of these peaks will become clear below.

The anion photoelectron spectra of $DI^-$ measured with 1064 and 532 nm photons using our magnetic bottle electron energy analyzer are shown in Fig. 2(b), and the electron binding energies of their peaks are summarized in Table II. Similarly to the case of $HI^-$, the 1064 nm photoelectron spectrum of $DI^-$ showed (0, 0)–(5, 0) peaks consistent with the known vibrational energy spacings of the neutral DI ($X\ ^1\Sigma^+$).[75] The 532 nm spectrum of $DI^-$ showed the same vibrational series but over an extended range to include the (0, 0)–(8, 0) transitions. The (4, 0) peak was obscured by an intense peak due to $D^-$. This was due to a two-photon process that resulted in the photodissociation of $DI^-$, followed by the photodetachment of $D^-$. The narrower vibrational energy spacings of DI, compared

**TABLE I.** Electron binding energies of the peaks in the MB-measured photoelectron spectra and VMI-measured photoelectron spectra of $HI^-$ (both for 1064 and 532 nm), the fitted anisotropy parameters, $\beta$, in the 1064 nm VMI-measured photoelectron spectrum, and their coefficients of determination, $R^2$. The values in parentheses in the $\beta$ column show the standard deviations. The electronic transition is HI ($X\ ^1\Sigma^+$) ← $HI^-$ ($X\ ^2\Sigma^+$).

| $HI^-$ well | ($v'$, $v''$) | MB (eV) 1064 nm | MB (eV) 532 nm | VMI (eV) 1064 nm | VMI (eV) 532 nm | $\beta$ 1064 nm | $R^2$ of $\beta$ 1064 nm |
|---|---|---|---|---|---|---|---|
| | | 0.003 | | | | | |
| Inner | (0, 0) | 0.057 | 0.071 | 0.051 | | 1.62(8) | 0.87 |
| Inner | (1, 0) | 0.323 | 0.324 | 0.319 | 0.307 | 1.87(5) | 0.95 |
| Inner | (2, 0) | 0.598 | 0.579 | 0.578 | 0.585 | 1.76(4) | 0.97 |
| Inner | (3, 0) | 0.854 | | 0.830 | | 1.74(4) | 0.96 |
| Inner | (4, 0) | | 1.086 | 1.077 | 1.081 | 1.81(7) | 0.91 |
| Inner | (5, 0) | | 1.332 | | 1.333 | | |
| Inner, outer | (6, 0) | | 1.544 | | 1.529 | | |
| Outer | (7, 0) | | 1.750 | | 1.752 | | |
| Outer | (8, 0) | | 1.938 | | 1.951 | | |
| Outer | (9, 0) | | 2.14 | | 2.15 | | |
| Outer | (10, 0) | | >2.304 | | >2.286 | | |
| | $H^-$ | | 0.758 | | 0.760 | | |

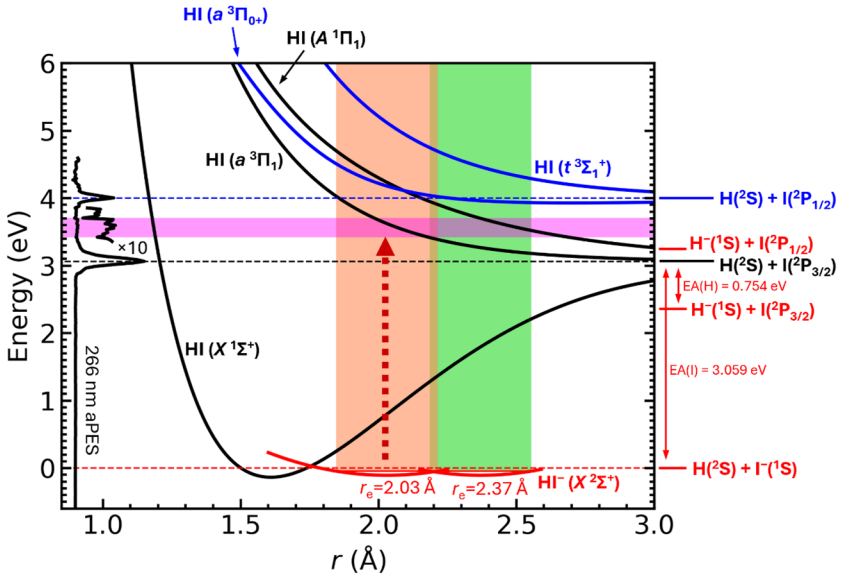


**FIG. 3.** Potential energy curves of $HI^-$/HI. The origin of the energy axis (0 eV) is the $H(^2S) + I^-(^1S)$ dissociation limit. The ground state potential of HI was taken from Ref. 71, and the excited state potentials of HI were taken from Ref. 22. The harmonic potentials of $HI^-$ (red) and their vibrational ground state are based on the present study and explained in Sec. III D. The orange-shaded area represents the Franck–Condon region of $HI^-$ due to the inner well ($r_e$ = 2.03 Å), and the green-shaded area represents that of $HI^-$ due to the outer well ($r_e$ = 2.37 Å). The 266 nm anion photoelectron spectrum (aPES) shown on the left is the same spectrum as in Fig. 5(b), and is plotted relative to the vibrational ground state of $HI^-$. The red dashed arrow represents the vertical transition of HI ($a\ ^3\Pi_1$) ← $HI^-$ ($X\ ^2\Sigma^+$, inner well), corresponding to the 3.64 eV feature (purple-shaded) of the 266 nm spectrum.

to those of HI, enabled interpretation of the peaks at energies beyond the first envelope of the (0, 0)–(8, 0) transitions. At electron binding energies beyond the (8, 0) peak, a second vibrational envelope appeared; these correspond to the transitions, (9, 0) through (12, 0). The observation of two envelopes corresponding to the same neutral DI ($X\ ^1\Sigma^+$) final electronic state indicates that $DI^-$ exists in *two forms*. One of these has a *short bond length* and is responsible for the (0, 0)–(8, 0) envelope, while the other has a *longer bond length* and is responsible for the (8, 0)–(12, 0), that is, the second envelope. The fact that the first and the second envelopes shared the (8, 0) peak indicates that the two forms of $DI^-$ are nearly *isoenergetic*. Taking this interpretation of $DI^-$ back to $HI^-$ in Fig. 2(a), the

**TABLE II.** Electron binding energies of the peaks in the MB-measured photoelectron spectra of $DI^-$ (1064 and 532 nm). The electronic transition is DI ($X\ ^1\Sigma^+$) ← $DI^-$ ($X\ ^2\Sigma^+$).

| $DI^-$ well | ($v'$, $v''$) | MB (eV) 1064 nm | MB (eV) 532 nm |
|---|---|---|---|
| Inner | (0, 0) | 0.028 | 0.059 |
| Inner | (1, 0) | 0.225 | 0.24 |
| Inner | (2, 0) | 0.426 | 0.42 |
| Inner | (3, 0) | 0.622 | 0.60 |
| Inner | (4, 0)/$D^-$ | 0.805 | 0.78 |
| Inner | (5, 0) | 0.993 | 0.949 |
| Inner | (6, 0) | | 1.108 |
| Inner | (7, 0) | | 1.31 |
| Inner, outer | (8, 0) | | 1.46 |
| Outer | (9, 0) | | 1.597 |
| Outer | (10, 0) | | 1.774 |
| Outer | (11, 0) | | 1.914 |
| Outer | (12, 0) | | 2.054 |

(0, 0)–(6, 0) peaks in the first envelope of the $HI^-$ spectrum originated from the shorter form of $HI^-$, while the (6, 0)–(9, 0) peaks in the second envelope of the $HI^-$ spectrum originated from the longer form of $HI^-$.

This information provides a rough picture of the $HI^-$ potential energy curve and its relationship to that of HI (see Fig. 3). $HI^-$ is predicted to have a bound potential ($X\ ^2\Sigma^+$) leading to the $H(^2S)$ + $I^-(^1S)$ dissociation asymptote, as well as dissociative potentials ($1\Omega_{1/2}$, $\Omega_{3/2}$) leading to the $H^-(^1S)$ + $I(^2P_{3/2})$ dissociation limit.[43,44,47] The $H^-(^1S)$ + $I(^2P_{3/2})$ limit is located $D_0$(HI) − EA(H) = 3.053 eV[77] − 0.754 eV[76] = 2.299 eV above the vibrational ground state of the neutral HI. Since the $HI^-$ photoelectron spectra showed the vibrational features of neutral HI starting from $v' = 0$, the $v'' = 0$ of $HI^-$ lies below $v' = 0$ of the neutral HI. Therefore, the $HI^-$ studied here is on the $X\ ^2\Sigma^+$ potential energy curve associated with the $H(^2S)$ + $I^-(^1S)$ limit. The existence of isoenergetic $HI^-$ with two different bond lengths means that $HI^-$ ($X\ ^2\Sigma^+$) has a *double-well potential*, with the vibrational wavefunction tunneling through the barrier between the two wells. Such tunneling is well known, such as the umbrella inversion of ammonia (barrier height ~0.22 eV).[78,79] It was also reported for some diatomic molecules, such as NaK, where the vibrational wavefunctions with energy close to the barrier height were delocalized over the two wells.[80,81] The overall shape of the $HI^-$ potential curve, reflecting this interpretation, is shown in Fig. 4(a). The energies of the vibrational ground states of the $HI^-/DI^-$ anions are based on the (0, 0) transitions in the anion photoelectron spectra (these being the EA-determining peaks), while the bond lengths at the two local minima of the double wells are based on the Franck–Condon simulations elaborated in Sec. III D. In the 532 nm photoelectron spectra of $HI^-$ and $DI^-$ (Fig. 2), the second envelope covers a narrower energy range than the first envelope. Part of the reason is the anharmonicity of the potential energy curve of the HI neutral, as illustrated in Fig. 8. However, the F–C simulations, which incorporate the anharmonicity of the HI neutral's potential, showed that the contribution from the anharmonicity is not enough to reproduce the narrow energy range of the second envelope. This fact indicates that the outer well of the $HI^-$ potential has a higher curvature (sharper) than the inner well; hence, the F–C region of the outer well is narrower than that of the inner well, as illustrated in Fig. 4(a). The specific shape of the curve and the height of the barrier are not determined in the present study. However, on the assumption that the potential barrier is below the H + $I^-$ dissociation limit, the estimated barrier height is of the order of ~0.1 eV, which is small enough for the vibrational wavefunction to tunnel. In a double-well potential, the vibrational state could experience doublet splitting by the even and odd combinations of the coupled vibrational wavefunctions of the two wells.[78,79] Thus, unresolved transitions may be present in the photoelectron spectra.

The raw EA values determined from the (0, 0) transition peaks were 0.057 ± 0.020 eV for HI and 0.028 ± 0.020 eV for DI [see Fig. S3



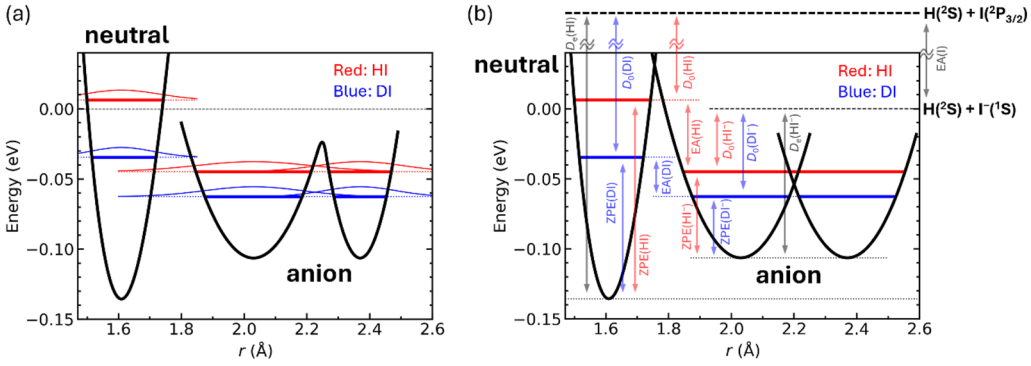


**FIG. 4.** (a) Potential energy curves of the HI/DI neutral and the $HI^-/DI^-$ anion, with the horizontal lines at their vibrational ground states. The origin of the energy axis (0 eV) is the $H(^2S)$ + $I^-(^1S)$ dissociation limit. The vibrational wavefunctions are overlaid to show that they tunnel through the barrier of the double-well potential of the anion. The vibrational ground states of the anions are based on the electron affinities determined by the photoelectron spectra, and the bond lengths of the anion at the two minima are based on the Franck–Condon simulations. The energies of the two minima and the barrier height of the anion's potential curve are not known. The potential of the neutral HI was taken from Ref. 71. (b) Potential energy curves of the HI/DI neutral and the $HI^-/DI^-$ anion, and the relationships of the electron affinity (EA), zero-point energy (ZPE), bond dissociation energy ($D_0$), and depth of the well ($D_e$) of each species. The two curves of the anion are the harmonic potentials $U(r) = (1/2)\ k_e\ (r - r_e)^2 - D_e$ used in the Franck–Condon simulations in Sec. III D.

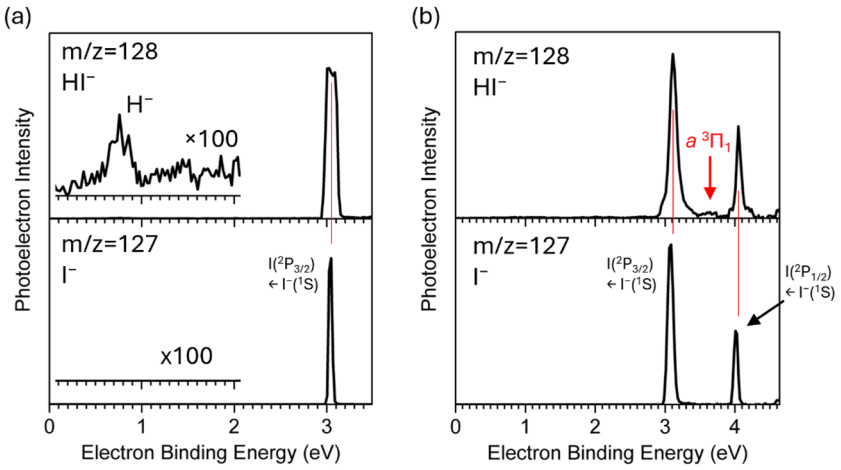


**FIG. 5.** Anion photoelectron spectra of $HI^-$ and $I^-$ recorded using (a) 355 nm (3.493 eV) photons and (b) 266 nm (4.661 eV) photons on our magnetic bottle electron energy analyzer. The electron binding energy of each peak is shown in Table III. The red vertical lines are for visual assistance.

**TABLE III.** Electron binding energies of the peaks in the MB-measured photoelectron spectra of $HI^-$ (355 and 266 nm).

| | MB (eV) 355 nm | MB (eV) 266 nm |
|---|---|---|
| $I(^2P_{3/2}) \leftarrow I^-(^1S)$ | 3.03 | 3.109 |
| $HI(a\ ^3\Pi_1) \leftarrow HI^-(X\ ^2\Sigma^+)$ | | 3.64 |
| $I(^2P_{1/2}) \leftarrow I^-(^1S)$ | | 4.048 |

in the supplementary material for the enlarged spectra in the vicinity of the (0, 0) peaks]. Further refinement of the EA values, which will involve incorporating VMI photoelectron results, will be discussed in Sec. III C. The (0, 0) peak of $HI^-$ in the 1064 nm spectrum exhibited a left shoulder at an electron binding energy of 0.003 eV. This peak is not due to the valence-bound $HI^-$ because this binding energy does not satisfy the thermodynamic requirement that the $HI^-$ vibrational ground state lies below the H + $I^-$ dissociation limit—i.e., EA(HI) > EA(I) − $D_0$(HI) = 6 meV.[40] The assignment of this peak will be discussed in Sec. IV B. This left-shoulder feature at an extremely low electron binding energy was not evident in the 532 nm spectrum because of the lower resolution at higher electron kinetic energies.

The anion photoelectron spectra of $HI^-$ and $I^-$, measured with 355 and 266 nm photons using our magnetic bottle analyzer, are shown in Fig. 5. In Fig. 5(b), $HI^-$ displayed two peaks at the electron binding energies of the $I(^2P_{3/2}) \leftarrow I^-(^1S)$ and $I(^2P_{1/2}) \leftarrow I^-(^1S)$ transitions, separated by the spin–orbit splitting of I.[58,77] These were due to the two-photon process by which $I^-$ was first formed by the photodissociation of $HI^-$ and subsequently photodetached. Between these two intense peaks, there is a small broad feature at ~3.64 eV. This feature was assigned to the transition from the inner well of $HI^-$ to HI ($a^3\Pi_1$) based on our Franck–Condon simulation results in Sec. III D. The electron binding energies of the observed peaks are presented in Table III. As shown in the inset of Fig. 5(a), the peak originating from the photodissociated $H^-$ fragment appeared in the 355 nm photoelectron spectrum at 0.760 eV, as it had in the 532 nm photoelectron spectrum.

### C. Anion photoelectron spectra measured by the velocity map imaging (VMI) electron energy analyzer

The use of our VMI analyzer, while recording the $HI^-$ photoelectron spectrum, provided both higher energy resolution than that provided by the MB analyzer and the measurement of the $HI^-$ photoelectron angular distribution (PAD). The raw images and the reconstructed images of $HI^-$ recorded with 1064 and 532 nm photons are presented in Figs. 6(a) and 6(b). The photoelectron signals appeared along the direction of the polarization of the photodetachment laser. The photoelectron spectra obtained from these images [Fig. 6(c)] are consistent with those obtained using the magnetic bottle analyzer [Fig. 2(a)]. When utilizing the VMI analyzer, the (4, 0) peak was observed at an electron binding energy of 1.086 eV in the 1064 nm ($h\nu$ = 1.165 eV) photoelectron spectrum, while when using the MB analyzer, it was not observed due to MB's poor electron transmission at low electron kinetic energies. The electron binding energies of the observed peaks are summarized in Table I. The raw EA value of HI based on the (0, 0) transition was 0.051 ± 0.015 eV. This is consistent with the EA value determined when using the MB analyzer, with the 0.051 eV datapoint from the VMI measurement falling between the highest 0.057 eV datapoint and the next highest 0.044 eV datapoint recorded with the MB analyzer, as shown in Fig. S3 in the supplementary material. Since the VMI analyzer provides better resolution and has smaller datapoint spacings, we report 0.051 ± 0.015 eV as the experimental EA value of HI. From a previous computational study, the electronic ground state of the anion is $HI^-$ ($X\ ^2\Sigma^+$, $1\sigma^2 2\sigma^2 1\pi^4 3\sigma^1$), where the extra electron is in the antibonding 3σ orbital.[43] The transition from the electronic ground state of the anion to its corresponding neutral ground state is HI ($X\ ^1\Sigma^+$) ← $HI^-$ ($X\ ^2\Sigma^+$), and the orbital angular momentum along the molecular axis is zero for both the anion and the neutral. Therefore, the EA values of HI and DI do not require spin–orbit correction. The rotational corrections to the EA values will be discussed in Sec. III D. The bond dissociation energies $D_0$ of $HI^-$ and $DI^-$ can be calculated using EA(HI) = 0.051(15) eV and EA(DI) = 0.028(20) eV, as determined from our photoelectron spectra, and the known values of EA(I) = 3.059 038(10) eV,[77] $D_0$(HI) = 3.052 74(37) eV,[82] ZPE(HI) = 0.141 911 eV,[75] and ZPE(DI) = 0.101 029 eV,[75] by

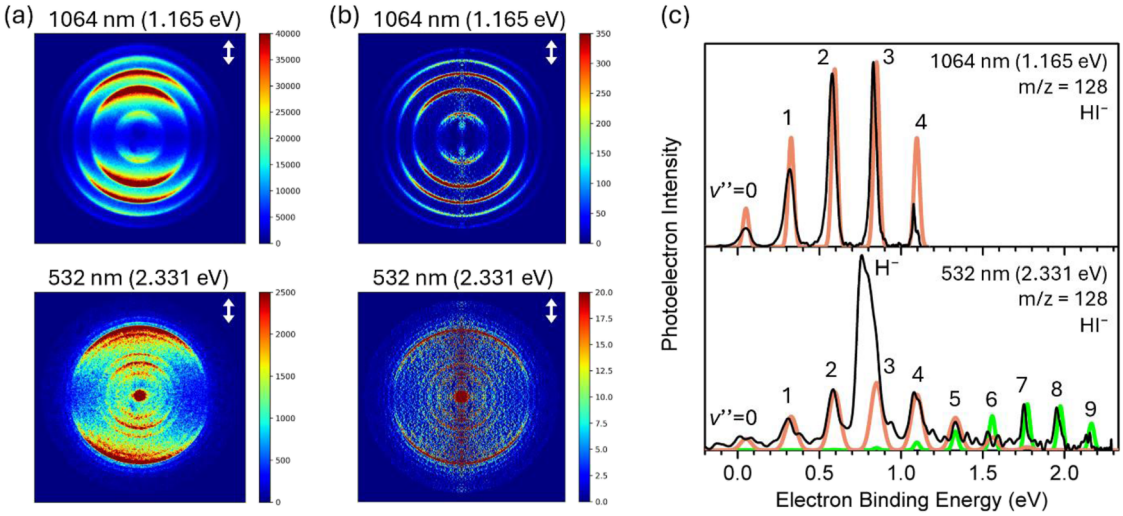


**FIG. 6.** (a) Raw velocity map images of $HI^-$ photoelectrons recorded with 1064 nm (1.165 eV) photons (top) and 532 nm (2.331 eV) photons (bottom). The white arrows in the images show the polarization direction of the photodetachment laser. The color scale represents the photoelectron counts. (b) Reconstructed velocity map images after symmetrization and inverse Abel transformation. The photoelectron angular distributions obtained from the 1064 and 532 nm images are presented in Fig. 7(a) and Fig. S4 in the supplementary material, respectively. (c) The black lines are the experimental spectra, and the electron binding energies of each of the peaks are shown in Table I. The orange curves show the results of Franck–Condon simulations for the transitions from $HI^-$ ($v'' = 0$) in the inner well ($r_e = 2.03$ Å) to HI ($X\,^1\Sigma^+$, $v'$). The green curves show the results of Franck–Condon simulations for the transitions from $HI^-$ ($v'' = 0$) in the outer well ($r_e = 2.37$ Å) to HI ($X\,^1\Sigma^+$, $v'$).

**TABLE IV.** The electron affinity (EA) values of HI/DI and the bond dissociation energy ($D_0$) values of $HI^-/DI^-$ determined by anion photoelectron spectra.

| | EA (eV) | $D_0$ of $HI^-/DI^-$ (eV) |
|---|---|---|
| HI | 0.051(15) | 0.045(15) |
| DI | 0.028(20) | 0.063(20) |

using the following energetic relationship [see Fig. 4(b) for visual assistance]:

$$D_0(HI^-) = D_0(HI) + EA(HI) - EA(I) \approx 0.045(15)\ \text{eV},$$

$$D_0(DI^-) = D_0(DI) + EA(DI) - EA(I),$$

$$= [D_0(HI) + ZPE(HI) - ZPE(DI)] + EA(DI) - EA(I),$$

$$\approx 0.063(20)\ \text{eV}.$$

These results are summarized in Table IV.

The photoelectron angular distribution (PAD) of each peak in the 1064 nm VMI-collected photoelectron spectrum is shown in Fig. 7(a). The observed PAD was fitted to the Cooper–Zare formula: $I(\theta) = a\,(1 + \beta\,P_2(\cos\theta))$, where $\theta$ is the angle between the direction of the ejected electron and the polarization of the incident light, $I(\theta)$ is the photoelectron intensity, $a$ is the constant proportional to the total photodetachment cross section, $\beta$ is the anisotropy parameter ranging from −1 to +2, and $P_2(\cos\theta)$ is the second-order Legendre polynomial [$P_2(\cos\theta) = (1/2)\,(3\cos^2\theta - 1)$].[83] The $\beta$ values obtained by least-squares fitting are presented in Table I and are plotted against electron kinetic energy (EKE) in Fig. 7(b). Since the five peaks in the 1064 nm spectrum originated from the same electronic transition—i.e., HI ($X\,^1\Sigma^+$) ← $HI^-$ ($X\,^2\Sigma^+$)—the $\beta$ dependences reflect the partial-wave channels of electron detachment at a given EKE.[83,84] Overall, $\beta$ being in the realm of 2 (p wave) over the entire observed EKE range indicates that the electrons are detached from a molecular orbital having s-character.[85] As shown in Fig. S4 in the supplementary material, the photoelectron counts in the 532 nm VMI-measured photoelectron spectrum were not reliable enough to achieve credible fittings of $\beta$.

### D. Franck–Condon simulation

Franck–Condon (F–C) simulations were performed to determine the bond lengths at the two minima in the double-well potential of $HI^-$. The potential energy curves of the anion and the neutral are needed to calculate the F–C factors using the LEVEL16 program. The generalized Morse potential from Ref. 71 was used for the HI neutral. For the potential energy curve of the anion, our photoelectron spectra implied that it has a double-well potential. However, quantum chemical calculations would be needed to map the shape of this curve accurately. Instead, we have modeled it using simple harmonic oscillator potentials, $U(r) = (1/2)\,k_e\,(r - r_e)^2 - D_e$, where the origin, 0 eV, was set at the $H(^2S) + I^-(^1S)$ dissociation limit for the anion. We then optimized the center of the harmonic well, $r_e$, to reproduce each of the two envelopes in the experimental anion photoelectron spectra. The force constant $k_e$ (the curvature of the well) and the depth of the well $D_e$ utilized in this simulation were determined as described below, using the harmonic approximation and the EA values of HI/DI. Since $k_e$ does not affect the binding energy center of the envelope, the same value was used for the two harmonic wells of the anion, for simplicity of the simulation. In the

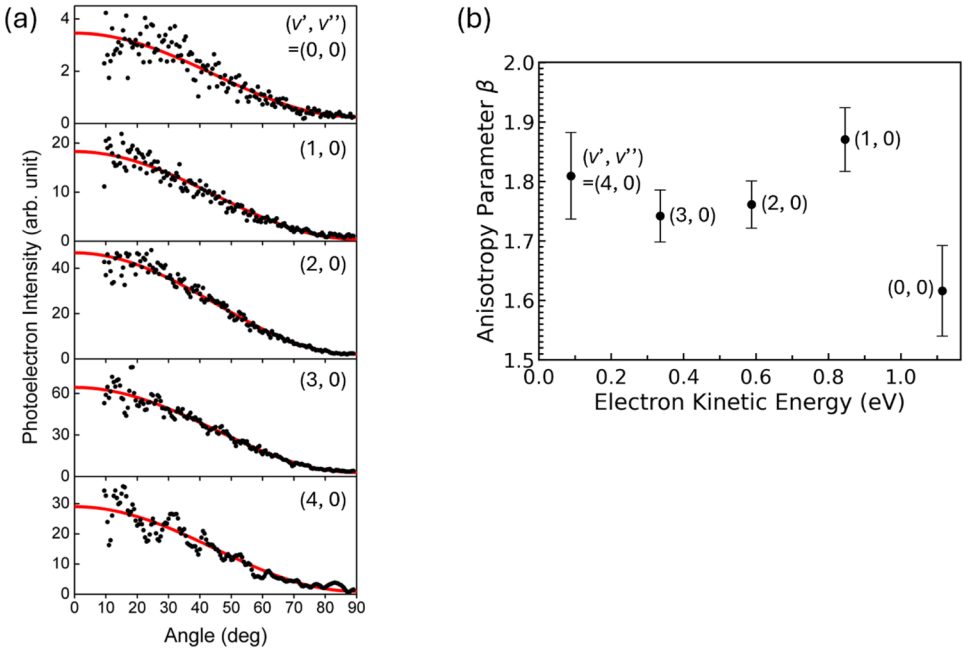


**FIG. 7.** (a) Photoelectron angular distribution (PAD) for each peak in the 1064 nm (1.165 eV) VMI-measured photoelectron spectrum of $HI^-$ (black), and their corresponding $I(\theta) = a\ (1 + \beta P_2(\cos\theta))$ fitted curves (red). (b) The fitted anisotropy parameters, $\beta$, in the 1064 nm VMI-measured photoelectron spectrum of $HI^-$ plotted against the electron kinetic energy (EKE). The error bars represent standard deviations. The $\beta$ values are presented in Table I.

harmonic potential of a diatomic molecule, the zero-point energy (ZPE), the vibrational constant, $\omega_e$, the force constant, $k_e$, and the reduced mass, $\mu$, have the following relationship:

$$\mathrm{ZPE} = \frac{1}{2}\hbar\omega_e = \frac{1}{2}\hbar\sqrt{\frac{k_e}{\mu}}. \tag{1}$$

Therefore, $\mathrm{ZPE}(DI^-)$ can be expressed in terms of $\mathrm{ZPE}(HI^-)$ by the following equation:

$$\frac{\mathrm{ZPE}(HI^-)}{\mathrm{ZPE}(DI^-)} = \sqrt{\frac{\mu_{DI}}{\mu_{HI}}},$$

$$\therefore\ \mathrm{ZPE}(DI^-) = \mathrm{ZPE}(HI^-)\sqrt{\frac{\mu_{HI}}{\mu_{DI}}}. \tag{2}$$

Using Eq. (2) and $\mathrm{ZPE}(HI^-) - \mathrm{ZPE}(DI^-) = D_0(DI^-) - D_0(HI^-) = 0.063–0.045$ eV $= 0.018$ eV [see Fig. 4(b) for visual assistance], $\mathrm{ZPE}(HI^-)$ can be determined as follows:

$$\mathrm{ZPE}(HI^-) - \mathrm{ZPE}(DI^-) = \mathrm{ZPE}(HI^-) - \mathrm{ZPE}(HI^-)\sqrt{\frac{\mu_{HI}}{\mu_{DI}}},$$

$$= \mathrm{ZPE}(HI^-)\cdot\left(1 - \sqrt{\frac{\mu_{HI}}{\mu_{DI}}}\right),$$

$$\mathrm{ZPE}(HI^-) = \frac{\mathrm{ZPE}(HI^-) - \mathrm{ZPE}(DI^-)}{1 - \sqrt{\frac{\mu_{HI}}{\mu_{DI}}}},$$

$$\approx 0.062\ \text{eV}.$$

Note that these values have uncertainties too large to be used as spectroscopic constants. They are used here only for convenience in determining the parameters of the harmonic potential for the F–C simulations. For example, the uncertainty in the values shown here is $\mathrm{ZPE}(HI^-) - \mathrm{ZPE}(DI^-) = 0.018 \pm 0.025$ eV and $\mathrm{ZPE}(HI^-) = 0.062 \pm 0.086$ eV. Using $\mathrm{ZPE}(HI^-) = 0.062$ eV and Eq. (2), $\mathrm{ZPE}(DI^-) \approx 0.044$ eV. From the energetic relationships shown in Fig. 4(b),

$$D_e(HI^-/DI^-) = D_0(HI^-) + \mathrm{ZPE}(HI^-) \approx 0.106\ \text{eV},$$

$$\omega_e(HI^-) = 2\ \mathrm{ZPE}(HI^-) = 995\ \text{cm}^{-1},$$

$$\omega_e(DI^-) = 2\ \mathrm{ZPE}(DI^-) = 707\ \text{cm}^{-1}.$$

The force constant $k_e$ can be calculated using Eq. (1):

$$k_e(HI^-/DI^-) = 4\mu_{HI^-}\left(\frac{\mathrm{ZPE}(HI^-)}{\hbar}\right)^2 = 58.3\ \text{N m}^{-1}.$$

In the harmonic potential of the anion, $U(r) = (1/2)\ k_e\ (r - r_e)^2 - D_e$, with $k_e = 58.3\ \text{N m}^{-1}$ and $D_e = 0.106$ eV, the only remaining parameter, $r_e$, was optimized to reproduce the experimental anion photoelectron spectra. The first envelope in the photoelectron spectra was reproduced with an anionic bond length of $r_e = 2.03$ Å, and the second envelope was reproduced with $r_e = 2.37$ Å. The simulated spectra are shown as the orange and green curves, respectively, in Figs. 2 and 6(c); the harmonic potentials used in the simulations are indicated in Figs. 3, 4(b), and 8, albeit on different scales; and the calculated F–C factors and the transition energy of each $(v', v'')$ peak are summarized in Tables S1–S4 in the supplementary material. Based on the observation of $I^-$ formation, previous experimental DEA studies on HI concluded that the potential energy curve of HI

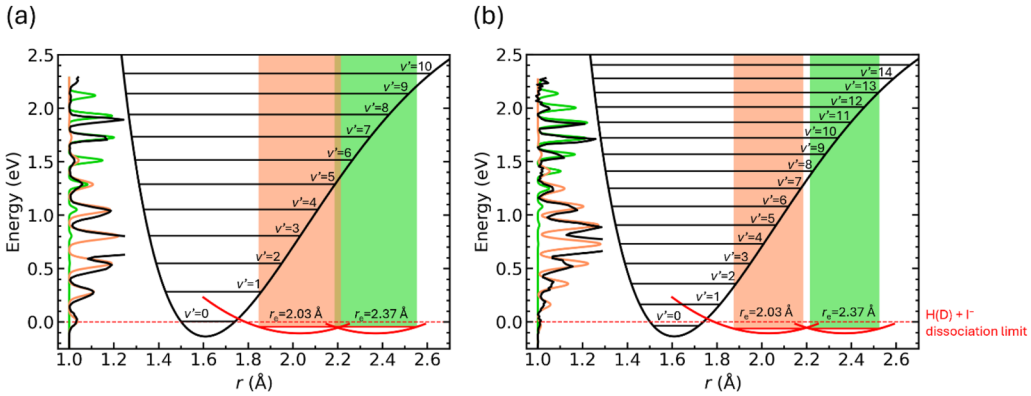


**FIG. 8.** (a) The extended Morse potential of HI (black, taken from Ref. 71) and the two harmonic potentials of $HI^-$ (red) used for our Franck–Condon (F–C) simulations. The vibrational levels of HI were taken from Ref. 75. The vibrational ground state of $HI^-$ is based on the EA(HI) determined in this study. The orange-shaded area represents the F–C region of the inner well of $HI^-$($r_e$ = 2.03 Å), and the green-shaded area represents that of the outer well ($r_e$ = 2.37 Å). The origin of the energy axis is the $H(^2S)$ + $I^-(^1S)$ dissociation limit. The 532 nm experimental anion photoelectron spectrum (black), the F–C simulation result for $HI^-$ in the inner well (orange), and that for $HI^-$ in the outer well (green) are the same as Fig. 2 and are plotted based on the vibrational ground state of $HI^-$. (b) The corresponding potential energy diagram and anion photoelectron spectrum of $DI^-$/DI.

crosses that of $HI^-$ at thermal energies (<0.1 eV).[43,45–47] The rough picture of the potential energy curve in Fig. 4 shows that all the barriers are <0.1 eV between the vibrational ground state of neutral HI and the vibrational ground state of $HI^-$.

Figure 3 shows the 266 nm photoelectron spectrum of $HI^-$ [the same spectrum as in the top panel of Fig. 5(b)] laid on its side on the potential energy diagram. It shows that the broad feature at ~3.64 eV in that photoelectron spectrum corresponds to the transition from $HI^-$ in its inner well ($r_e$ = 2.03 Å) to the excited electronic state of HI ($a\ ^3\Pi_1$). Dissociative photodetachment often forms broad peaks in anion photoelectron spectra, as shown in Refs. 86 and 87 for $O_4^- + h\nu \rightarrow 2\,O_2 + e^-$ and in Ref. 88 for $HOCO^- + h\nu \rightarrow H + CO_2 + e^-$ or $OH + CO + e^-$. Thus, the broad feature at ~3.64 eV is consistent with the assignment whereby $HI^-$ (in its inner well) undergoes dissociative photodetachment through the HI ($a\ ^3\Pi_1$) repulsive potential energy curve to yield $H(^2S) + I(^2P_{3/2}) + e^-$. As shown in Fig. S2 in the supplementary material, the electronic configurations of both HI ($X\ ^1\Sigma^+$, $1\sigma^2 2\sigma^2 1\pi^4$) and HI ($a\ ^3\Pi_1$, $1\sigma^2 2\sigma^2 1\pi^3 3\sigma^1$)[32] are accessible from $HI^-$ ($X\ ^2\Sigma^+$, $1\sigma^2 2\sigma^2 1\pi^4 3\sigma^1$)[43] by photodetaching the 3σ and the 1π electron, respectively. In a previous photodissociation study, neutral HI was excited to its $v$ = 2 vibrational level to widen the F–C region so as to probe the excited electronic states over a wider geometrical range.[24] The anion photoelectron spectrum of $HI^-$ obtained here mapped the excited state of HI at $r$ = 2.03 Å, which is much longer than the bond length of the ground-state neutral HI ($r_e$ = 1.609 16 Å[75]).

The rotational constants, $B_e = \hbar^2/(2\mu r_e^2)$, of $HI^-$ and $DI^-$ at the two bond lengths ($r_e$ = 2.03 and 2.37 Å) identified by the F–C simulations are shown in Table V. The corrections to the EA values due to the unresolved rotational manifolds in the photoelectron peaks can be estimated using these rotational constants and the estimated rotational temperature of the anion. Our RET anion source is similar to that of Compton *et al.*[41] In their REMPI measurements, the HI molecular beam formed by supersonic expansion had a rotational temperature of ~20 (±10) K and appreciably occupied only states with $J \leq 3$, these having an average rotational energy of ~1.4 meV. Although we do not know the rotational distribution of the $HI^-/DI^-$ anions after Rydberg electron transfer from $K^{**}(8d)$, we estimated the rotational corrections to the EA values using a rotational temperature of 20 K. The electron kinetic energy (EKE) band shift due to an unresolved rotational manifold for a linear molecule is expressed by the following formula: $\Delta_{rot} \approx k_B T(B'/B'' - 1) + (1/3)(B'' - B')$.[89,90] Using the estimated rotational temperature $T$ = 20 K, the anion rotational constants $B''$ derived here, and the known neutral rotational constants $B'$ (6.426 365 0 $cm^{-1}$ for HI and 3.253 487 2 $cm^{-1}$ for DI[75]), the rotational corrections to the EA values of HI and DI were obtained and are listed in Table V. For the EA values of HI and DI, that is, EA(HI) = 51 ± 15 meV and EA(DI) = 28 ± 20 meV, as determined from the (0, 0) photoelectron peaks originating from their inner wells, the rotational corrections were −0.89 meV for HI and −0.94 meV for DI. These are much smaller than our energy resolution and are practically negligible.

**TABLE V.** Rotational constants $B_e$ of $HI^-/DI^-$ and rotational corrections to the EAs of HI/DI.

| | Inner well ($r_e$ = 2.03 Å) | | Outer well ($r_e$ = 2.37 Å) | |
|---|---|---|---|---|
| | $HI^-$ | $DI^-$ | $HI^-$ | $DI^-$ |
| Rotational constant $B_e$ | 4.09 $cm^{-1}$ | 2.06 $cm^{-1}$ | 3.00 $cm^{-1}$ | 1.51 $cm^{-1}$ |
| Rotational correction to EA | −0.89 meV | −0.94 meV | −1.8 meV | −1.9 meV |

## IV. DISCUSSION

### A. Comparison with previous studies of $HI^-$

In this section, we examine the consistency of our results with those from previous observations of $HI^-$. In the first report of the experimental observation of $HI^-$ using a Penning discharge ion source by Chupka *et al.*, their assumption of $HI^-$ to be a stable anion set the lower limit for the EA value to be EA(HI) > EA(I) − $D_0$(HI) = 6 meV,[40] using the currently accepted values of EA(I) = 3.059 038(10) eV[77] and $D_0$(HI) = 3.052 74(37) eV.[82] The EA(HI) = 51 ± 15 meV obtained by our work satisfies this requirement.

Compton *et al.* formed $HI^-$ via Rydberg electron transfer using several alkali metals $M^{**}$ (M = Na, Rb, and Cs).[41] They set the lower limit for EA(HI) by the energetic requirement that the HI + $M^{**}$ collision energy, $E_{collision}$, needed to be high enough to enable electron transfer from $M^{**}$ to HI: $E_{collision}$ > BE($M^{**}$) − EA(HI), where BE($M^{**}$) is the binding energy of the Rydberg electron in $M^{**}$.[41] Out of the excited alkali atoms, $M^{**}$ that they utilized to produce $HI^-$, the one with the largest BE was $Rb^{**}$(9s), with BE = 0.39 eV. The collision energy was $E_{collision}$ < 0.26 eV in their experimental conditions. These values lead to a lower limit for EA(HI) to be EA(HI) > BE($Rb^{**}$) − $E_{collision}$ = 0.13 eV. Here, we reexamine this energetic requirement using the values from the present HI + $K^{**}$ experiments. In our experiments, the Rydberg level of $K^{**}$ with the largest BE was 8d (BE = 0.227 eV[58,75]). With EA(HI) = 0.051 eV, the requirement for the collision energy is $E_{collision}$ > BE($K^{**}$) − EA(HI) = 0.176 eV. Under our experimental conditions, all of the HI + $K^{**}$ collisions satisfy this requirement. The evaluation of the collision energy in our experimental setup is detailed in the supplementary material. Therefore, the experimental results presented here are consistent with the observations by Compton *et al.*[41]

Next, we compare our experimental results with the *ab initio* calculations on $HI^-$ by Chapman *et al.*[43] In the RCA and SOCI calculations, the potential well of $HI^-$ ($X\,^2\Sigma^+$) was predicted to be around $r_e$ = 2.65 Å with a vibrational constant of $\omega_e$ = 352 $cm^{-1}$ and a well depth of $D_e$ = 0.10–0.16 eV. The bond lengths we obtained in the present study ($r_e$ = 2.03 Å for the inner well, $r_e$ = 2.37 Å for the outer well) were much shorter than their prediction. In the SOCI calculation with the diffuse H atom basis, the potential energy curve of $HI^-$ was predicted to have a small well around 1.6 Å, which is close to the bond length of the HI neutral.[43] Perhaps this might be a reflection of the double-well nature of the $HI^-$ potential energy curve. In any case, we believe that our work provides a more accurate determination of the pertinent bond lengths.

Later, theoretical studies using the nonlocal resonance model were conducted[50–52] based on the available *ab initio* computational results[43] and the experimental DEA HI results using low-energy electrons (0–170 meV).[49] That work predicted the resonance potential of $HI^-$ to have a double well, although the energies and the bond lengths at its two minima are different from our results, likely due to the availability of only limited experimental information at the time. That work showed that the resonance potential for $HI^-$ has a bound state at bond length >1.7 Å and merges with that of neutral HI around $r$ = 1.74 Å,[50] which is consistent with our observations as shown in Fig. 4. They predicted the $HI^-$ potential as to have a barrier around 2.1 Å and an outer well that is wider than the inner well. This was partly the case, because they fit their model to reproduce the wide well around $r_e$ = 2.65 Å, which had been predicted by the *ab initio* calculation.[43] Nevertheless, the overall picture of a double-well potential for $HI^-$, based on the nonlocal resonance model[50–52] and on DEA experiments,[49] is consistent with our experimental results. This analysis should be revisited to incorporate the present anion photoelectron results.

Furthermore, another theoretical study of $HCl^-$ and $HBr^-$ predicted that these systems should have double-well potentials separated by barriers formed by avoided crossings between their H + $X^-$ potential and the HX + $e^-$ continuum.[91]

### B. Non-valence-bound $HI^-$ anion with an extremely low electron binding energy

As shown in Fig. 2(a) and Fig. S3(a) in the supplementary material, the (0, 0) peak in the 1064 nm MB-photoelectron spectrum of $HI^-$ exhibited a weak but persistent shoulder-like feature at an electron binding energy of ~0.003 eV. This is essentially 0 eV at our resolution. This spectral feature was reproduced in repeated measurements on separate days. Its presence raises the possibility that $HI^-$ may exist not only as the valence-bound anion as discussed above, but also as a non-valence-bound anion. Note in Fig. 2(b) and Fig. S3(b) in the supplementary material that the low electron binding energy side of the (0, 0) peak in the 1064 nm MB-photoelectron spectrum of $DI^-$ may also be exhibiting the same feature, just less clearly and with broadening. Two major classes of non-valence-bound anions are dipole-bound anions (DBA)[57,92–95] and quadrupole-bound anions (QBA).[57,94,95] For the former, the critical dipole moment required to capture an electron is 1.625 D[96] as computed theoretically and ~2.5 D as estimated experimentally.[97,98] Since the dipole moment of HI is 0.4477 D,[99] and since it monotonically decreases as the bond length is elongated toward the anion's geometry,[100–102] HI cannot form a DBA in either its neutral or its anion geometries. On the other hand, the quadrupole moment of HI increases as it is elongated from its neutral bond length (3.3 $ea_0^2$ at $r_e$ = 1.6092 Å) to a maximum of 4.4 $ea_0^2$ at $r$ ~ 2.4 Å.[102] Thus, HI in its anion geometries has a larger quadrupole moment than it does in its neutral geometry. Based on the quadrupole moment function in Ref. 102, neutral HI should have a quadrupole moment of 4.1 $ea_0^2$ at $r$ = 2.03 Å (the bond length of the anion's inner well) and 4.4 $ea_0^2$ at 2.37 Å (the bond length of the anion's outer well). It is worth noting that the quadrupole moment of HI reaches its maximum around the bond length of the anion's outer well. Unfortunately, there is no widely known critical quadrupole moment criterion for capturing an electron. If the ~0.003 eV peak that arises on the low EBE side of the (0, 0) peak originates from a quadrupole-bound $HI^-$, then there are at least two possible explanations for its formation. One is for a neutral HI molecule to capture an excess electron while its H–I bond is elongated during vibration, forming a nascent $HI^-$ quadrupole-bound anion (QBA) that then acts as a "doorway" or "stepping stone" state, leading to the valence-bound anion.[103] It sometimes occurs that both a multipole-bound anion and a valence-bound anion of the same molecule are observed in the same anion photoelectron spectrum.[103] Another possibility is that the $HI^-$ QBA is formed when a valence-bound $HI^-$ in the outer well loses its extra electron to the continuum. In that case, the leaving electron may be

recaptured by the maximal quadrupole moment of HI to form the QBA. Examination of whether these scenarios are possible is within the reach of theory.[104,105]

While the non-valence-bound anion peak appeared in the 1064 nm MB-anion photoelectron spectrum, it was not observed in the 1064 nm VMI-photoelectron spectrum [Fig. 6(c) and Fig. S3(a) in the supplementary material] despite its better energy resolution. For anions with such low electron binding energies, the effect of background blackbody radiation from the walls of the apparatus cannot be ignored. For example, Dunning *et al.* reported that the lifetime of the acetonitrile DBA (EA ~22 meV[92,93]) was limited to 70–85 μs due to photodetachment induced by the blackbody radiation at 300 K.[106–108] Although the photon number density in an ideal blackbody cavity depends only on the temperature, the radiation field in the actual apparatus is not uniform due to temperature gradients. Here, we consider the effect of the radiation field of an ideal blackbody cavity at 300 K (room temperature) for simplicity. The photon number density distribution as a function of photon energy was derived and is shown in Fig. S7 in the supplementary material. Almost 100% (>99.7%) of the photons from blackbody radiation have energy higher than 3 meV, and 60% of them have energy higher than 51 meV. Therefore, while both the non-valence-bound $HI^-$ (BE 3 meV) and the valence-bound $HI^-$ (BE 51 meV) are photodetached over time by the blackbody radiation from the apparatus, the decay rate of the non-valence-bound $HI^-$ is ~1.7 times higher than that of the valence-bound $HI^-$. In our apparatus, along the TOF-MS flight tube, the photodetachment region of the VMI analyzer is located downstream of the MB-analyzer. In our experiments, it took ~14 μs for $HI^-$ with a kinetic energy of 1500 eV (defined by the TOF-MS extraction voltage) to fly from the photodetachment region of the MB analyzer to the VMI analyzer. The longer flight time to the VMI analyzer led to the reduced intensity of non-valence-bound $HI^-$ anions because blackbody radiation depletes the non-valence-bound $HI^-$ more rapidly than the valence-bound $HI^-$. This may be the reason the 0.003 eV peak was observed only in the MB-photoelectron spectrum, while it was not observed in the VMI-photoelectron spectrum. As a note, when the anion intensity is strong enough, our VMI analyzer can record the spectra of weakly bound anions such as the acetonitrile DBA;[93] that is, it can accept the ion intensity losses. Thus, with the strong ion intensity of $HI^-$ in the mass spectrum, it is not surprising that the VMI-photoelectron spectrum of the valence-bound $HI^-$ was recorded despite its BE of 51 meV falling within the range of blackbody radiation anion depletion.

### C. Comparison with alkali halide anions, $MX^-$

Comparison of the anion photoelectron spectra of $HI^-$ with those of alkali halide anions, $MX^-$ (M = Li, Na, K, Rb, Cs; X = F, Cl, Br, I),[109,110] provides insight into its bonding nature. These are qualitatively analogous systems. In the discussion below, we use $KI^-$ as an example of $MX^-$, because photodetached electrons from both the SOMO and SOMO−1 were observed in anion photoelectron spectra by Lineberger *et al.*[109] and Smalley *et al.*[110] The same discussion can be applied to other $MX^-$ species.

With the alkali metals being hydrogen-like atoms, the transition between the ground electronic states of the anions and those of their corresponding neutrals can be represented as $X\ ^1\Sigma^+ \leftarrow X\ ^2\Sigma^+$ for both $HI^-$ and $KI^-$. As shown in Fig. 9, the SOMO of the anion would be the σ* orbital, consisting of the p orbital of the I atom and the s orbital of the H/K atom. Photodetachment from this orbital gives rise to the EA-determining peaks in the anion photoelectron spectra of $HI^-$ at 0.051 eV and of $KI^-$ at 0.728 eV.[109] The SOMO−1 is the π orbital originating from the p orbital of the I atom. Photodetachment from this orbital appeared in the photoelectron spectrum of $HI^-$ at 3.64 eV and in the spectrum of $KI^-$ at 4.3 eV.[110] Despite the similarity between $HI^-$ and $KI^-$, the EA value of HI (0.051 eV) determined here is much smaller than the EA values of MX (0.4–0.9 eV). Also, $HI^-$ does not follow the linear relationship between the EA and $\alpha_M/r_{MX}^2$ ($\alpha_M$: polarizability of M, $r_{MX}$: bond length of MX) that is seen for alkali halides.[109] This can be explained by the different nature of the σ* SOMO in $HI^-$ compared to that in $KI^-$. In the case of $KI^-$, the σ* orbital is localized on the K atom because it has a much larger contribution from the s orbital of the K atom than from the p orbital of the I atom [Fig. 9(b)]. In addition, the K atom has a large polarizability (42.9 $Å^3$[111]) and a much smaller electronegativity (0.82 on Pauling's scale[112]) than the I atom (2.66[112]). These properties of $KI^-$ are largely consistent with an electrostatic model of $(e^-K^+)\ I^-$, where the SOMO electron on the K atom, that is, $e^-\ldots K^+$, is highly polarized away from $I^-$.[109] In this model, the $I^-$ is stabilized by its Coulomb attraction with $(e^-\ldots K^+)$.[110] This stabilization effect can be quantified using the binding energies of the p electrons in $I^-$. These binding energies are 4.3 eV for $KI^-$,[109] and 3.059 eV (EA of I) for $I^-$.[77] Therefore, in $KI^-$, the Coulomb stabilization effect on the $I^-$ part is 4.3–3.059 eV = 1.2 eV. In the case of $HI^-$, the s orbital of the H atom and the p orbital of the I atom are located at comparable energies, and the σ* orbital has contributions from both atomic orbitals [Fig. 9(a)]. Therefore, the σ* orbital of $HI^-$ has covalent character and is delocalized over the molecule, compared to

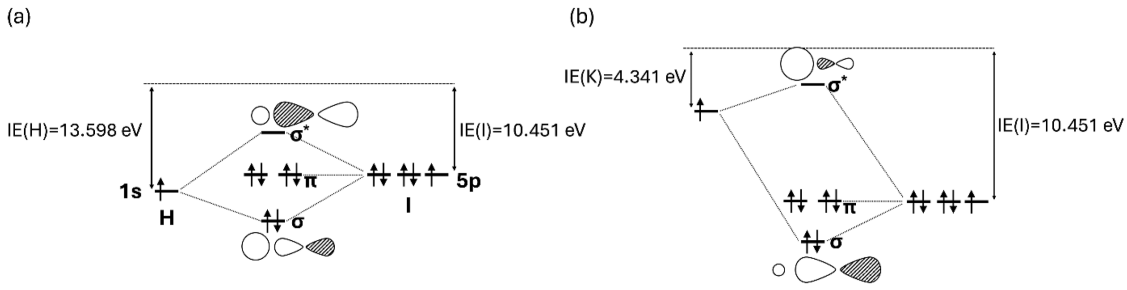


**FIG. 9.** LCAO-MO diagrams for (a) HI and (b) KI. The sizes of the s and p atomic orbitals qualitatively show their contributions to the molecular orbitals. The ionization energies (IEs) are based on the NIST database.[75]

that of $KI^-$, which has ionic character and is localized on the K atom. The electron binding energy of the $\sigma^*$ electron in $HI^-$ does not follow the linear relationship with $\alpha_M/r_{MX}^2$ as in $MX^-$, because of the fundamental difference in their bonding characters. In addition, the polarizability of the H atom (0.668 Å$^3$[111]) is two orders of magnitude smaller than that of the K atom (42.9 Å$^3$[111]), and the electronegativity of the H atom (2.2 in Pauling's scale[112]) is comparable to that of the I atom (2.66[112]). Therefore, the H atom in $HI^-$ is not as polarized as the K atom in $KI^-$, and the bonding picture of $HI^-$ is thus covalent, $[H–I]^-$, rather than ionic, $(e^-H^+)\,I^-$. The electron binding energy shift, i.e., stabilization, for photoelectrons from the p orbital of $I^-$ in $HI^-$ is 3.64 eV − EA(I) = 0.6 eV. The Coulomb stabilization effect of $I^-$ in $HI^-$ is much smaller than the stabilization effect of $I^-$ in $KI^-$, because the H atom in $HI^-$ is not as polarized as the K atom in $KI^-$.

In summary, the $\sigma^*$ SOMO of $HI^-$ has covalent character as opposed to the ionic character of the alkali halide anion, $MX^-$. The $\pi$ SOMO−1 orbitals of $HI^-$ and $MX^-$ have similar character, with dominant contributions from the p orbital of the halogen atom.

## V. CONCLUSIONS

The properties of $HI^-$ and $DI^-$ were probed by anion photoelectron spectroscopy. The measured electron affinities were EA(HI) = 0.051 ± 0.015 eV and EA(DI) = 0.028 ± 0.020 eV. Using these values, the bond dissociation energies were determined to be $D_0(HI^-)$ = 0.045 ± 0.015 eV and $D_0(DI^-)$ = 0.063 ± 0.020 eV. $HI^-$ has a double-well potential with two minima at the bond lengths, $r_e$ = 2.03 Å and $r_e$ = 2.37 Å, and with its vibrational wavefunction ranging over the two wells by tunneling through the barrier. This is the first spectroscopic study performed on $HI^-/DI^-$ anions. Previous theoretical studies[43,50–52] and interpretations of DEA experimental results[44–52] faced challenges due to the lack of such spectroscopic data. In addition to $HI^-/DI^-$ valence-bound anions, the observation of extremely low-binding-energy peaks indicated the formation of non-valence-bound anions, perhaps as quadrupole-bound anions. Comparison of the anion photoelectron spectra of $HI^-$ with those of the alkali halides, $MX^-$, emphasized the covalent character of the H–I bond.

## SUPPLEMENTARY MATERIAL

See the supplementary material for anion photoelectron spectra (MB and VMI) of calibrants at 1064 nm photon energy (Fig. S1); molecular orbital diagrams of $HI^-/HI/HI^+$ (Fig. S2); the 1064 nm aPES of $HI^-$ (MB and VMI) and $DI^-$ (MB) magnified around the (0, 0) peaks (Fig. S3); photoelectron angular distributions in the 532 nm VMI-aPES of $HI^-$ (Fig. S4); experimental results using HCl and HBr instead of HI (Fig. S5); evaluation of the requirement for the HI + $K^{**}$ collision energy (Fig. S6); evaluation of the blackbody radiation from the walls of the apparatus (Fig. S7); and the Franck–Condon factors and the anion-to-neutral transition energies output by the LEVEL16 program (Tables S1–S4).

## ACKNOWLEDGMENTS

This material is based on work supported by the National Science Foundation (NSF) and the Air Force Office of Scientific Research (AFOSR) under Grant Nos. CHE-2054308 (K.H.B.) and FA9550-22-1-0271 (K.H.B.), respectively. We benefited from several conversations with the late Bob (R.N.) Compton before embarking on this work.

## AUTHOR DECLARATIONS

### Conflict of Interest

The authors have no conflicts to disclose.

### Author Contributions

**Tatsuya Chiba**: Formal analysis (equal); Investigation (equal); Visualization (equal); Writing – original draft (equal). **Burak A. Tufekci**: Investigation (equal); Writing – original draft (supporting). **Shiying Wang**: Investigation (equal). **Yuheng Han**: Investigation (equal). **Kit H. Bowen**: Conceptualization (lead); Funding acquisition (lead); Investigation (lead); Methodology (lead); Project administration (lead); Resources (lead); Supervision (lead); Validation (lead); Writing – review & editing (lead).

## DATA AVAILABILITY

The data that support the findings of this study are available from the corresponding author upon reasonable request.

## REFERENCES

[1] D. C. Frost, C. A. McDowell, and D. A. Vroom, J. Chem. Phys. **46**, 4255 (1967).
[2] H. J. Lempka, T. R. Rassmore, and W. C. Price, Proc. R. Soc. A **304**, 53 (1968).
[3] C. E. Brion and P. Crowley, J. Electron Spectrosc. Relat. Phenom. **11**, 399 (1977).
[4] T. A. Carlson, P. Gerard, M. O. Krause, G. Von Wald, J. W. Taylor, and F. A. Grimm, J. Chem. Phys. **84**, 4755 (1986).
[5] L. Karlsson, S. Svensson, P. Baltzer, M. Carlsson-Göthe, M. P. Keane, A. N. de Brito, N. Correia, and B. Wannberg, J. Phys. B: At., Mol. Opt. Phys. **22**, 3001 (1989).
[6] A. Mank, M. Drescher, T. Huth-Fehre, G. Schönhense, N. Böwering, and U. Heinzmann, J. Electron Spectrosc. Relat. Phenom. **52**, 661 (1990).
[7] P. Baltzer, L. Karlsson, S. Svensson, and B. Wannberg, J. Phys. B: At., Mol. Opt. Phys. **23**, 1537 (1990).
[8] A. Mank, M. Drescher, T. Huth-Fehre, N. Böwering, U. Heinzmann, and H. Lefebvre-Brion, J. Chem. Phys. **95**, 1676 (1991).
[9] N. Böwering, H.-W. Klausing, M. Müller, M. Salzmann, and U. Heinzmann, Chem. Phys. Lett. **189**, 467 (1992).
[10] M. Y. Adam, M. P. Keane, N. de Brito, N. Correia, B. Wannberg, P. Baltzer, L. Karlsson, and S. Svensson, Chem. Phys. **164**, 123 (1992).
[11] C. J. Zietkiewicz, Y.-Y. Gu, A. M. Farkas, and J. G. Eden, J. Chem. Phys. **101**, 86 (1994).
[12] A. J. Cormack, A. J. Yencha, R. J. Donovan, K. P. Lawley, A. Hopkirk, and G. C. King, Chem. Phys. **221**, 175 (1997).
[13] A. J. Yencha, M.-W. Ruf, and H. Hotop, Z. Phys. D: At., Mol. Clusters **29**, 163 (1994).
[14] D. J. Hart and J. W. Hepburn, Chem. Phys. **129**, 51 (1989).
[15] J. H. D. Eland and J. Berkowitz, J. Chem. Phys. **67**, 5034 (1977).
[16] C. E. Brion, I. E. McCarthy, I. H. Suzuki, E. Weigold, G. R. J. Williams, K. L. Bedford, A. B. Kunz, and R. Weidman, J. Electron Spectrosc. Relat. Phenom. **27**, 83 (1982).
[17] M. A. Young, J. Phys. Chem. **97**, 13508 (1993).
[18] S. T. Pratt, J. Chem. Phys. **101**, 8302 (1994).
[19] C. F. Goodeve and A. W. C. Taylor, Proc. R. Soc. London, Ser. A **154**, 181 (1936).
[20] W. C. Price, Proc. R. Soc. London, Ser. A **167**, 216 (1938).
[21] B. J. Huebert and R. M. Martin, J. Phys. Chem. **72**, 3046 (1968).
[22] R. J. Le Roy, G. T. Kraemer, and S. Manzhos, J. Chem. Phys. **117**, 9353 (2002).

[23]S. Manzhos, H.-P. Loock, B. L. G. Bakker, and D. H. Parker, J. Chem. Phys. **117**, 9347 (2002).
[24]J. P. Camden, H. A. Bechtel, D. J. A. Brown, A. E. Pomerantz, R. N. Zare, and R. J. Le Roy, J. Phys. Chem. A **108**, 7806 (2004).
[25]D. R. J. Boyd and H. W. Thompson, Spectrochim. Acta **5**, 308 (1952).
[26]S. C. Hurlock, R. M. Alexander, K. R. Rao, and S. N. Dreska, J. Mol. Spectrosc. **37**, 373 (1971).
[27]J. M. Cherlow, H. A. Hyatt, and S. P. S. Porto, J. Chem. Phys. **63**, 3996 (1975).
[28]E. D. Palik, J. Chem. Phys. **23**, 217 (1955).
[29]M. Cowan and W. Gordy, Phys. Rev. **104**, 551 (1956).
[30]F. C. De Lucia, P. Helminger, and W. Gordy, Phys. Rev. A **3**, 1849 (1971).
[31]K. V. Chance, T. D. Varberg, K. Park, and L. R. Zink, J. Mol. Spectrosc. **162**, 120 (1993).
[32]A. B. Alekseyev, H.-P. Liebermann, D. B. Kokh, and R. J. Buenker, J. Chem. Phys. **113**, 6174 (2000).
[33]N. Balakrishnan, A. B. Alekseyev, and R. J. Buenker, Chem. Phys. Lett. **341**, 594 (2001).
[34]A. Brown, Int. J. Quantum Chem. **107**, 2665 (2007).
[35]D. A. Chapman, K. Balasubramanian, and S. H. Lin, Chem. Phys. Lett. **118**, 192 (1985).
[36]D. N. Jodoin and A. Brown, J. Chem. Phys. **123**, 054301 (2005).
[37]A. Brown, J. Chem. Phys. **122**, 084301 (2005).
[38]D. A. Armstrong and J. L. Holmes, "Decomposition of halides and derivatives," in *Compherensive Chemical Kinetics, Volume 4, Decomposition of Inorganic and Organometallic Compounds*, edited by C. H. Bamford and C. F. H. Tipper (Elsevier Publishing Company, Amsterdam, 1972), pp. 155–174.
[39]L. G. Christophorou, D. L. McCorkle, and A. A. Christodoulides, "Electron attachment process," in *Electron–Molecule Interactions and Their Applications*, edited by L. G. Christophorou (Acdemic Press, Inc., Orlando, FL, 1984), Vol. 1, pp. 511–515.
[40]D. Spence, W. A. Chupka, and C. M. Stevens, J. Chem. Phys. **76**, 2759 (1982).
[41]H. S. Carman, Jr., C. E. Klots, and R. N. Compton, J. Chem. Phys. **99**, 1734 (1993).
[42]A. A. Tuinman and R. N. Compton, Rapid Commun. Mass Spectrom. **10**, 389 (1996).
[43]D. A. Chapman, K. Balasubramanian, and S. H. Lin, Phys. Rev. A **38**, 6098 (1988).
[44]Y. L. Coat, R. Azria, and M. Tronc, J. Phys. B: At. Mol. Phys. **18**, 809 (1985).
[45]N. G. Adams, D. Smith, A. A. Viggiano, J. F. Paulson, and M. J. Henchman, J. Chem. Phys. **84**, 6728 (1986).
[46]D. Smith and N. G. Adams, J. Phys. B: At. Mol. Phys. **20**, 4903 (1987).
[47]S. H. Alajajian and A. Chutjian, Phys. Rev. A **37**, 3680 (1988).
[48]A. Chutjian, S. H. Alajajian, and K.-F. Man, Phys. Rev. A **41**, 1311 (1990).
[49]D. Klar, B. Mirbach, H. J. Horsch, M.-W. Ruf, and H. Hotop, Z. Phys. D **31**, 235 (1994).
[50]J. Horáček, W. Domcke, and H. Nakamura, Z. Phys. D **42**, 181 (1997).
[51]J. Horáček, M. Čížek, and W. Domcke, Theor. Chem. Acc. **100**, 31 (1998).
[52]J. Horáček, K. Houfek, and M. Čížek, Phys. Rev. A **75**, 022719 (2007).
[53]D. Spence and T. Noguchi, J. Chem. Phys. **63**, 505 (1975).
[54]M. Schmeisser, in *Handbook of Preparative Inorganic Chemistry*, 2nd ed., edited by G. Brauer (Academic Press, New York, 1963), Vol. 1, pp. 286–289.
[55]T. Chiba, J. A. Olaniyan, S. Wang, Y. Han, E. Miliordos, and K. H. Bowen, J. Phys. Chem. A **129**, 9676 (2025).
[56]S. M. Ciborowski, R. M. Harris, G. Liu, C. J. Martinez-Martinez, P. Skurski, and K. H. Bowen, Jr., J. Chem. Phys. **150**, 161103 (2019).
[57]G. Liu, S. M. Ciborowski, J. D. Graham, A. M. Buytendyk, and K. H. Bowen, J. Chem. Phys. **151**, 101101 (2019).
[58]A. Kramida, Y. Ralchenko, and J. Reader,, and NIST ASD Team, *NIST Atomic Spectra Database, V. 5.12* (National Institute of Standards and Technology, 2024).
[59]V. Dribinski, A. Ossadtchi, V. A. Mandelshtam, and H. Reisler, Rev. Sci. Instrum. **73**, 2634 (2002).
[60]C. S. Feigerle, R. R. Corderman, and W. C. Lineberger, J. Chem. Phys. **74**, 1513 (1981).
[61]X. Chen and C. Ning, J. Chem. Phys. **145**, 084303 (2016).
[62]C. S. Feigerle, R. R. Corderman, S. V. Bobashev, and W. C. Lineberger, J. Chem. Phys. **74**, 1580 (1981).
[63]M. Scheer, C. A. Brodie, R. C. Bilodeau, and H. K. Haugen, Phys. Rev. A **58**, 2051 (1998).
[64]R. C. Bilodeau, M. Scheer, and H. K. Haugen, J. Phys. B: At., Mol. Opt. Phys. **31**, 3885 (1998).
[65]A. O. Lindahl, P. Andersson, C. Diehl, O. Forstner, P. Klason, and D. Hanstorp, Eur. Phys. J. D **60**, 219 (2010).
[66]D. D. Laun and C. H. Corliss, J. Res. Natl. Bur. Stand., Sect. A **72**, 609 (1968).
[67]J. Ho, K. M. Ervin, and W. C. Lineberger, J. Chem. Phys. **93**, 6987 (1990).
[68]J. W. Rabalais, "Photoionization processes," in *Principles of Ultraviolet Photoelectron Spectroscopy* (Wiley, 1977), pp. 53–56.
[69]D. W. Arnold, S. E. Bradforth, T. N. Kitsopoulos, and D. M. Neumark, J. Chem. Phys. **95**, 8753 (1991).
[70]R. J. Le Roy, J. Quant. Spectrosc. Radiat. Transfer **186**, 167 (2017).
[71]J. A. Coxon and P. G. Hajigeorgiou, J. Mol. Spectrosc. **150**, 1 (1991).
[72]E. P. Wigner, Phys. Rev. **73**, 1002 (1948).
[73]S. Geltman, Phys. Rev. **112**, 176 (1958).
[74]M. Peper, F. Helmrich, J. Butscher, J. A. Agner, H. Schmutz, F. Merkt, and J. Deiglmayr, Phys. Rev. A **100**, 012501 (2019).
[75]P. J. Linstrom and W. G. Mallard, NIST Chemistry Webbook, NIST Standard Reference Database Number 69 (National Institute of Standards and Technology, 2023).
[76]K. R. Lykke, K. K. Murray, and W. C. Lineberger, Phys. Rev. A **43**, 6104 (1991).
[77]D. Hanstorp and M. Gustafsson, J. Phys. B: At., Mol. Opt. Phys. **25**, 1773 (1992).
[78]L. A. Veguilla-Berdecía, J. Chem. Educ. **70**, 928 (1993).
[79]A. M. Halpern, B. R. Ramachandran, and E. D. Glendening, J. Chem. Educ. **84**, 1067 (2007).
[80]A. Pashov, W. Jastrzebski, and P. Kowalczyk, J. Phys. B: At., Mol. Opt. Phys. **33**, L611 (2000).
[81]L. Morgus, P. Burns, R. D. Miles, A. D. Wilkins, U. Ogba, A. P. Hickman, and J. Huennekens, J. Chem. Phys. **122**, 144313 (2005).
[82]B. Ruscic and D. H. Bross, Active Thermochemical Tables (ATcT) values based on ver. 1.220 of the Thermochemical Network (Argonne National Laboratory, 2025), https://atct.anl.gov/Thermochemical%20Data/version%201.220/index.php
[83]J. Cooper and R. N. Zare, J. Chem. Phys. **48**, 942 (1968).
[84]J. L. Hall and M. W. Siegel, J. Chem. Phys. **48**, 943 (1968).
[85]A. Sanov, Annu. Rev. Phys. Chem. **65**, 341 (2014).
[86]L. A. Posey, M. J. Deluca, and M. A. Johnson, Chem. Phys. Lett. **131**, 170 (1986).
[87]M. J. DeLuca, C.-C. Han, and M. A. Johnson, J. Chem. Phys. **93**, 268 (1990).
[88]T. G. Clements, R. E. Continetti, and J. S. Francisco, J. Chem. Phys. **117**, 6478 (2002).
[89]P. C. Engelking, J. Phys. Chem. **90**, 4544 (1986).
[90]M. J. Travers, D. C. Cowles, and G. B. Ellison, Chem. Phys. Lett. **164**, 449 (1989).
[91]M. Čížek and J. Horáček, Int. J. Mass Spectrom. **280**, 149 (2009).
[92]C. G. Bailey, C. E. H. Dessent, M. A. Johnson, and K. H. Bowen, Jr., J. Chem. Phys. **104**, 6976 (1996).
[93]S. M. Ciborowski, G. Liu, J. D. Graham, A. M. Buytendyk, and K. H. Bowen, Eur. Phys. J. D **72**, 139 (2018).
[94]C. Desfrançois, Y. Bouteiller, J. P. Schermann, D. Radisic, S. T. Stokes, K. H. Bowen, N. I. Hammer, and R. N. Compton, Phys. Rev. Lett. **92**, 083003 (2004).
[95]G. Liu, S. M. Ciborowski, C. R. Pitts, J. D. Graham, A. M. Buytendyk, T. Lectka, and K. H. Bowen, Phys. Chem. Chem. Phys. **21**, 18310 (2019).
[96]O. H. Crawford and W. R. Garrett, J. Chem. Phys. **66**, 4968 (1977).
[97]K. R. Lykke, R. D. Mead, and W. C. Lineberger, Phys. Rev. Lett. **52**, 2221 (1984).
[98]N. I. Hammer, R. J. Hinde, R. N. Compton, K. Diri, K. D. Jordan, D. Radisic, S. T. Stokes, and K. H. Bowen, J. Chem. Phys. **120**, 685 (2004).
[99]K. P. Huber and G. Herzberg, *Molecular Spectra and Molecular Structure. IV. Constants of Diatomic Molecules* (Van Nostrand Reinhold Company, 1979).
[100]J. F. Ogilvie, W. R. Rodwell, and R. H. Tipping, J. Chem. Phys. **73**, 5221 (1980).

[101]H. Riris, C. B. Carlisle, D. E. Cooper *et al.*, J. Mol. Spectrosc. **146**, 381 (1991).
[102]J. F. Harrison, J. Chem. Phys. **128**, 114320 (2008).
[103]G. Liu, S. M. Ciborowski, J. D. Graham, A. M. Buytendyk, and K. H. Bowen, J. Chem. Phys. **153**, 044307 (2020).
[104]M. V. N. A. Prasad, R. F. Wallis, and R. Herman, Phys. Rev. B **40**, 5924 (1989).
[105]A. Ferrón, P. Serra, and S. Kais, J. Chem. Phys. **120**, 8412 (2004).
[106]L. Suess, Y. Liu, R. Parthasarathy, and F. B. Dunning, Chem. Phys. Lett. **376**, 376 (2003).
[107]L. Suess, Y. Liu, R. Parthasarathy, and F. B. Dunning, J. Chem. Phys. **119**, 12890 (2003).
[108]M. Cannon, Y. Liu, L. Suess, and F. B. Dunning, J. Chem. Phys. **128**, 244307 (2008).
[109]T. M. Miller, D. G. Leopold, K. K. Murray, and W. C. Lineberger, J. Chem. Phys. **85**, 2368 (1986).
[110]Y. A. Yang, L. A. Bloomfield, C. Jin, L. S. Wang, and R. E. Smalley, J. Chem. Phys. **96**, 2453 (1992).
[111]P. Schwerdtfeger and J. K. Nagle, Mol. Phys. **117**, 1200 (2019).
[112]National Center for Biotechnology Information, Electronegativity in the periodic table of elements; https://pubchem.ncbi.nlm.nih.gov/periodic-table/electronegativity